University of Bristol - Explore Bristol Research
General rights

Experimental quantification of noise in linear ultrasonic imaging

Rhodri L.T. Bevan, Jie Zhang, Nicolas Budyn, Anthony J. Croxford and Paul D. Wilcox

Abstract—An efficient procedure for experimental-based quantification of statistical distributions of both the random and micro-structural speckle noise within an ultrasonic image is presented. This is of particular interest in the multi-view total focusing method, which enables many images (views) of the same region to be obtained by utilising alternative ray paths and mode conversions. For example, in an immersion configuration, 21 separate views of the same region of a sample can be formed by exploiting direct and skip paths. These views can be combined through some form of data fusion algorithm, to improve defect detection and characterization performance. However, the noise level is different in different views and this should be accounted for in any data fusion algorithm. It is shown that by using only one set of experimental data from a single measurement location, rather than numerous independent locations, it is possible to obtain accurate noise parameters at an imaging level. This is achieved by accounting for the spatial variation in the noise parameters within the image, due to beam spread, directivity and attenuation with a simple empirical correction. An important feature of the process is the suppression of image artefacts caused by signal responses from other ray paths with the use of image masking. This masking process incorporates knowledge of the expected auto-correlation length (ACL) of image speckle noise and high amplitude cluster suppression. The expected ACL is determined via a simple ray-based forward model of a single point scatterer. Compared to the estimates obtained using multiple independent locations, the speckle noise parameters estimated from a single measurement location were within 0.4dB.

Index Terms—Noise measurement, ultrasonic imaging, ultrasonic transducer arrays

I. BACKGROUND

Ultrasonic inspection is utilised to detect and characterise defects within a structure in order to ensure the standard of manufacture and protect against failures over its lifetime. Success of the inspection to detect a defect, when present, is dependent on the operator's ability to separate and distinguish the defect signal from the background noise.

Although an ultrasonic inspection may be undertaken using a single transducer, a more advanced approach utilises a phased array system. The timing of transmission from individual phased array elements can be controlled, together with the overall firing pattern, resulting in a steered or focused wavefront which is targeted at a desired location, improving resolution at the focal point. However, this requires foreknowledge of the potential defect location. An alternative inspection routine for such systems, outlined by Holmes *et al.* [1] is

called full matrix capture (FMC). In FMC, A-scan data from all possible combinations of transmitter and receiver elements from the array are recorded individually. This allows for separation between the data capture procedure and the imaging approach, as no physical steering or focusing is undertaken. Instead, synthetic focusing can be achieved by applying the necessary timing delays via the appropriate algorithm in post-processing.

Ultrasonic imaging algorithms post-process the raw inspection data to provide visual assessment of the captured signal data. Numerous algorithms exist, ranging from the sector B-scan through to the total focusing method (TFM). A detailed discussion of different imaging algorithms is beyond the scope of this paper, for further information see [2]. The TFM is flexible and generalisable [3]–[5] since it allows for focusing in both transmission and reception, at all points within the image, using the linear delay-and-sum beamforming approach. In [6], indirect beamforming was presented for the TFM, increasing the amount of imaging data extracted from a single FMC by considering multiple ray paths to form additional images. This allows for the formation of multiple views of the same region of interest, which is termed multi-view TFM.

Noise in an ultrasonic image comes from various sources and can be broken down into two types, namely random and coherent noise. Whilst random noise can be suppressed through use of repeated signal capture and averaging, coherent noise will persist. Random noise must still be quantified to ensure adequate suppression.

Micro-structure induced coherent noise is typically the limiting factor in the ability to detect a defect, as such noise displays similar spectral characteristics to that of defect signals. This has led to significant research into improving the signal-to-noise ratio present in the underlying data through techniques such as adaptive beamforming [7]–[10]. Theoretical work on micro-structure induced noise on an imaging level was undertaken by Burckhardt [11] for B-scan imaging with emphasis on compounding. Spatial compounding, as a means of suppressing speckle noise was also investigated experimentally by Trahey *et al.* [12]. Experimental work by Wagner *et al.* [13], examined the statistical properties of ultrasonic speckle as a means of deducing underlying material (tissue) properties for medical diagnosis. Another method of suppression (adaptive speckle reduction filter) was considered by Crawford *et al.* [14], for medical B-scan imaging, although complete suppression is not possible.

There is significant research interest in utilising data fusion for non-destructive evaluation (NDE) [15]–[17]. Data fusion is the procedure of combining multiple datasets to provide more

insight and knowledge than possible from a single source or image. In the context of the current paper, the interest is in data fusion applied to multi-view TFM images of the same region of a component. It is advantageous to account for differing signal-to-noise ratios in the images being fused to avoid the procedure reducing resolution and detectability, the inverse of its intended goal. The focus of the paper is quantifying the noise levels and associated statistical distributions present in different TFM images from different views. It is a necessary step for determining the inspection limit for any conventional array inspection as well as in providing reliable signal to noise estimates for data fusion.

The overall aim is to determine an efficient and robust way of quantifying noise and its spatial variation within each image using as few defect-free FMC datasets as possible. Apart from a very simple model of random noise, the main motivation for the work is to avoid the need to have a complex physics-based model of coherent noise. To do this, the noise is firstly characterised using many FMC datasets to understand the noise distributions and how many parameters are needed to describe them; these are termed the "true" noise parameters. It is then assessed whether it is possible to accurately recover the true parameters from a lesser number of FMC datasets.

In the following section, the multi-view TFM algorithm is outlined. The remaining sections outline the theoretical approach for experimental characterisation of the random and coherent material noise together with the procedure for extracting this information from example data.

II. EXPERIMENTAL CONFIGURATION AND MULTI-VIEW TFM IMAGING METHOD

The multi-view TFM algorithm [6] extends the standard TFM. As in the standard method, it utilises a ray-based model of wave propagation. The use of different ray paths and wave modes enables different views of the same physical region to be generated from a single FMC dataset. The inspection configuration considered here is shown in figure 1a, with the region of interest (ROI) highlighted in green. In this work, the ROI extent is between x=[50mm,85mm] and z=[2mm,24.5mm]. This configuration is common across a range of industries for the inspection of welds in safety-critical components, with the ROI containing the weld. Although the work of Zhang *et al.* was applied to a contact inspection, the terminology of direct view, half-skip and full-skip to represent three ray path cases are equally relevant to an immersion setup. In the case of a skip view, the ray includes a reflection off the backwall of the specimen. In a half-skip view, this occurs once (either in transmit or receive), whilst in the full-skip case, both the transmit and receive rays include this backwall reflection. Since the ray can mode convert between transverse, T, and longitudinal, L, at a material boundary, these three cases are subdivided further to account for all possible mode combinations along the ray path. This is demonstrated in figure 1 for rays originating at the transmitter element T_x, travelling to the focus point and returning to the receiving element R_x.

As the transmit ray path may be different from the receive path, the notation used in this paper is as follows: A dash is

(a) Inspection setup
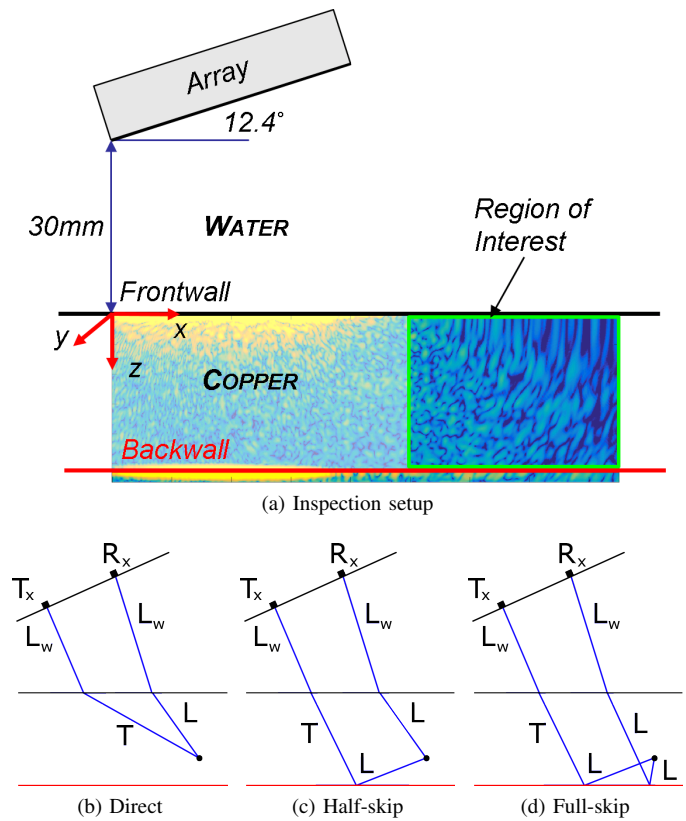

(b) Direct   (c) Half-skip   (d) Full-skip

Fig. 1. (a) Immersed oblique inspection setup and multi-view ray path examples of a (b) direct (T-L), (c) half-skip (TL-L) and (d) full skip (TL-LL) view

used to separate the transmit (left hand side) from the receive path (right). For example, $TL - L$ (figure 1c) denotes a half-skip view with the transmit path containing two legs inside the specimen, the first is a transverse mode from the frontwall to the backwall, the second leg is the longitudinal mode from the backwall to the focus point. On the return path, there is only one leg (direct) of longitudinal mode. This notation, when applied to an immersed inspection, does not include the water leg of either the transmit or receive paths, as only the longitudinal mode is possible on this leg, so is implicit.

Considering all potential mode conversions and allowing for a maximum of one backwall reflection per path, there are 6 possible paths L, T, LL, LT, TL, TT. For each path, the intersection(s) at the interface(s) can be determined via Fermat's principle [18]. The total travel time τ is the sum of the outbound and inbound travel times. The 6 potential paths for the transmit and receive rays result in 36 possible TFM images for an immersed specimen, only 21 of which are unique due to reciprocity (i.e. $TL - L \equiv L - LT$).

Post data collection, the raw FMC data is filtered and Hilbert transformed in the frequency domain using a Gaussian window function centred at the phased array centre frequency and -40dB half-bandwidth of 90% relative to the centre frequency. The image is then generated using the summation of the time-delayed data

$$I(\mathbf{r}) = \sum_{i=1}^{n} \sum_{j=1}^{n} a_{ij} \tilde{f}_{ij}(\tau_{ij}(\mathbf{r})) \tag{1}$$

where $\mathbf{r}$ represents the image pixel location, $\tilde{f}_{ij}$ the filtered, Hilbert-transformed FMC data with i denoting transmitter element, j the receiver element and n the number of elements in the phased array. a_{ij} denotes an optional apodisation term. The standard TFM applied here utilises uniform weighting, $\mathbf{a} = 1$.

In this work, an immersed copper specimen was inspected using the experimental setup (figure 1a and table I). Copper was selected for its high grain noise at the ultrasonic frequency of interest, making it a suitable material to assess noise characterisation capabilities. The probe consisted of a 5MHz linear 1D phased array with 128 elements and pitch of 0.3mm. The copper sample measured $200 \times 300 \times 26.5$mm in the x, y and z directions respectively. The experimental properties were determined by measuring the water temperature and material thickness. From the water temperature, the water velocity is determined. The material velocities were calculated from the backwall signal response.

TABLE I
EXPERIMENTAL PROPERTIES

Probe vertical standoff	30.0 mm
Probe inclination angle	12.4 °
Water velocity	1471.3 m/s
Instrument delay	630 ns
Copper thickness	26.5 mm
Copper L velocity	4755.9 m/s
Copper T velocity	2288.5 m/s

An example of the 21 multi-view TFM images obtained from a single FMC dataset from the copper specimen is presented in figure 2. This copper sample contains no defects, thus any signal response is due to either the material itself or signals associated with the frontwall ($z = 0$) and backwall ($z = 26.5$mm) features. In the L-L view, it is apparent that strong signals are coincident with both the backwall and the frontwall locations. In the L-T view however, an imaging artefact is present as a horizontal region of high amplitude, located at z=17mm below the array. Artefacts such as this are due to a signal response from another ray path (in this case the L-L backwall) appearing in the current view and reconstructing at the wrong point. In the T-T view, the ROI to the right of the probe is contaminated with the signal from the second frontwall reflection. The impact of imaging artefacts in the region of interest can be reduced through adjustment of the experimental setup, although complete elimination of artefacts in all views is challenging in practice. As imaging artefacts are themselves coherent, their presence will impact on the quantification of the coherent grain noise, thus a procedure to mask their presence will be presented in section III-C.

To determine the true noise characteristics at every position in every TFM image, without making any prior assumptions about its spatial variation within an image, it is necessary to utilise multiple independent defect-free FMC datasets. Here, such independent data is used to provide a benchmark to which more efficient noise-estimation techniques are compared. The measurement independence of different FMC datasets was assessed at the imaging level using the Pearson correlation coefficient. Multiple measurements were undertaken along a

traverse in the y-direction (perpendicular to the array) along the copper block. The Pearson coefficient was determined for every possible y location combination using

$$\rho_p(\mathbf{X}, \mathbf{Y}) = \frac{E[\mathbf{XY}] - E[\mathbf{X}]E[\mathbf{Y}]}{\sqrt{E[\mathbf{X}^2] - [E[\mathbf{X}]]^2}\sqrt{E[\mathbf{Y}^2] - [E[\mathbf{Y}]]^2}} \quad (2)$$

where $\mathbf{X}$ and $\mathbf{Y}$ denote two image samples and E is the expectation. These $\rho_p(\mathbf{X}, \mathbf{Y})$ coefficients are then categorised based on the y translation distance between them. Figure 3 shows a box plot of the correlation coefficients for every possible combination. In the box plot, the red line indicates the median correlation coefficient, the blue box denotes the interquartile range (25th to 75th quartile) for the location combination in question and the whiskers represent $\pm 2.7s$ from the median, where s is the standard deviation. The crosses denote outliers. The traverse was 46mm in length, with an incremental distance of 1mm. From the figure, it can be seen that the Pearson coefficient rapidly diminishes to low values as the spacing between measurements is increased. The conservative option of a 15mm offset between sampling locations was chosen, as this is also the array element length in the y-direction.

III. IMAGE NOISE CHARACTERISATION

Since image noise contains both coherent and incoherent contributions it is necessary to examine them individually. Sources of random, incoherent, noise include thermal and electrical instrumentation noise. Whilst the effect of random noise can be suppressed through use of repeated signal capture and averaging, it is necessary to quantify the random noise present in order to assess the suppression required.

Once the random noise within an image is adequately suppressed, the defect-free images will then be dominated by coherent noise, with this consisting of speckle noise due to the micro-structure and image artefacts as shown in figure 2. In this paper, the focus is on the ability to detect defects in artefact-free regions within a TFM image. Therefore the characterisation of noise in each view requires (a) random noise assessment (b) identification of regions containing artefacts and (c) identifying a suitable parameterisation that describes the speckle noise in the artefact-free part of the region of interest.

A. Random noise

Quantification of the random noise level requires a minimum of two FMC datasets captured under identical instrumental setups at the same position on a sample. The two successive FMC datasets after being filtered and Hilbert transformed can be written as

$$\tilde{f}_{ij}^{(1)}(t) = \tilde{f}_{ij}^{(0)}(t) + \tilde{n}_{ij}^{(1)}(t) \quad (3)$$

$$\tilde{f}_{ij}^{(2)}(t) = \tilde{f}_{ij}^{(0)}(t) + \tilde{n}_{ij}^{(2)}(t) \quad (4)$$

where $\tilde{f}_{ij}^{(0)}(t)$ is the underlying random-noise-free FMC data and the $\tilde{n}_{ij}^{(b)}(t)$ is the realisation of random noise present in dataset b. Hence the differenced data is

$$g_{ij}(t) = \tilde{f}_{ij}^{(2)}(t) - \tilde{f}_{ij}^{(1)}(t) = \tilde{n}_{ij}^{(2)}(t) - \tilde{n}_{ij}^{(1)}(t) \quad (5)$$
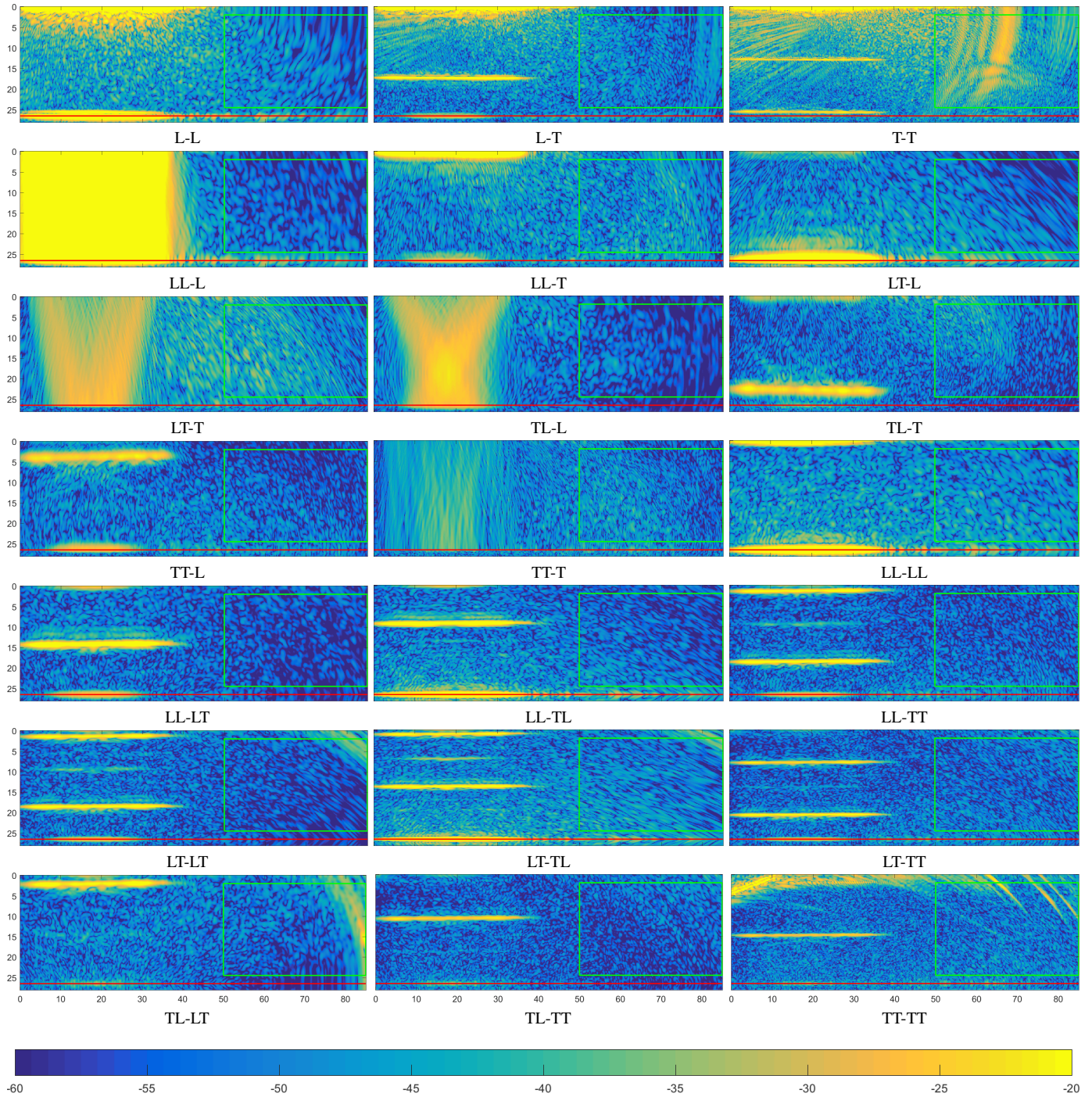
Fig. 2. Experimental example of the 21 unique TFM views (in dB) for immersed defect-free copper sample, considering only direct, half-skip and full-skip ray paths. The plot markings are consistent with figure 1a

It is hypothesised that the noise is normally distributed in the real and imaginary components of $g_{ij}(t)$. Examining only the real component initially, if the noise distribution in a single dataset is $N(0, \sigma_{ij}^2(t))$, then the distribution in $g_{ij}(t)$ is $N(0, 2\sigma_{ij}^2(t))$, following the difference of independent normal distributions [19]. It is assumed that no bias is present in the data due to the element combination pair or the sample time itself, therefore $\sigma_{ij}(t)$ is assumed to be constant and equal to σ_m. If a bias is present, then the random noise would need

to be assessed based on an individual matrix component level. Assuming $g_{ij}(t)$ contains uncorrelated, independent data, then every real component of the A-scan in the dataset will have the same normal distribution with variance $2\sigma_m^2$. This is also the case for the imaginary component. Probability plots of the real and imaginary components of $g_{ij}(t)$ are shown in figure 4. The probability plot assesses the discrete dataset against a theoretical distribution, in this case a normal distribution. If the discrete (empirical) cumulative distribution function (CDF)
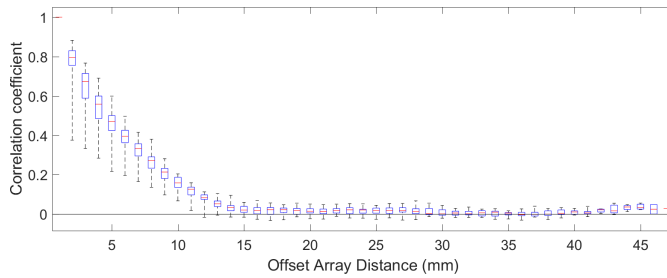
Fig. 3. Box plot of the Pearson correlation coefficient against traverse y-distance between combination. For each combination, the red line denotes the median correlation value, the blue box is the interquartile range and whiskers signify data extent

is a realisation of the theoretical distribution, the probability plot will be a straight line along y = x if the theoretical CDF is used on the y-axis. However it is usual to label the equivalent quantile information on the y-axis rather than the theoretical CDF values. The expected relationship is denoted by the dashed black line. The theoretical (normal) distribution parameter, σ_m, is obtained from the maximum likelihood estimator of the variance of $g_{ij}(t)$

$$\sigma_m = \sqrt{\frac{1}{4n^2T}\sum_{i=1}^{n}\sum_{j=1}^{n}\int_{t=0}^{T}|g_{ij}(t)|^2} \qquad (6)$$

where T is the time period in each A-scan in $g_{ij}(t)$. The data points in figure 4 denote amplitudes of the real and imaginary components of time samples from every A-scan within the FMC. From the figure, both components of $g_{ij}(t)$ are seen to be normally distributed and they are both found to have the same variance.
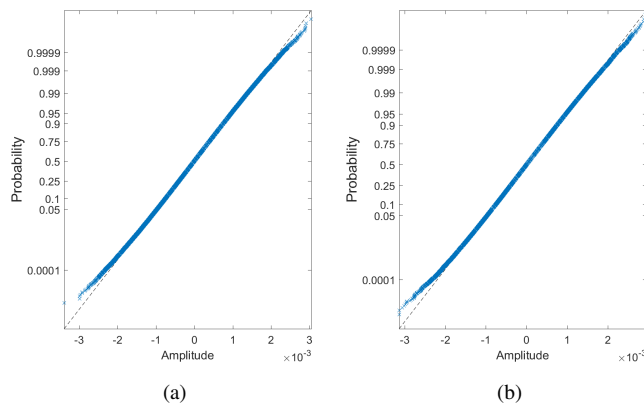

Fig. 4. Normal distribution probability plots for (a) real and (b) imaginary components of residual random noise after the subtraction of two consecutive filtered and Hilbert-transformed FMC datasets

At the imaging level, the random noise is dependent on the algorithm employed. With uniform apodisation in equation 1 and the assumption that each A-scan contains independent noise distributions with the same noise variance due to the lack of bias, the resulting image will have random noise with normally-distributed real and imaginary components $I_R = N(0, \sigma^2)$ and $I_I = N(0, \sigma^2)$ where $\sigma^2 = n^2\sigma_m^2$. This means

that, assuming I_R and I_I are independent, the TFM image noise intensity $|I| = |I_R + iI_I|$ has a Rayleigh distribution [20]

$$R(\sigma) = \frac{|I|}{\sigma^2}\exp-\frac{|I|^2}{2\sigma^2} \qquad (7)$$

A more practical measure of the image noise intensity is the Root Mean Square (RMS) noise level, $I_{RMS} = \sigma\sqrt{2}$, which can be estimated from N samples as $I_{RMS} = \sqrt{\frac{1}{N}\sum_{k=1}^{N}|I|^2}$. After N_a averages, the single A-scan variance is σ_m^2/N_a. Therefore, for a desired I_{RMS} the number of averages required is

$$N_a = \frac{2n^2\sigma_m^2}{I_{RMS}^2} \qquad (8)$$

with the standard deviation σ_m obtained from equation 6. In this work, $N_a = 20$.

B. Coherent grain noise

Speckle noise is due to interactions of the transmitted signal with the micro-structure of the material. As such, it is inherent to the specimen and cannot be suppressed by averaging. As the transmitted signal interacts with the grains (of random size and distribution), back-scattered signals result at the grain boundaries. The grains are too numerous and small to be resolvable at ultrasonic wavelengths, resulting in a superposition of signals that form a speckle pattern. In ultrasonic imaging, speckle noise intensity is Rayleigh distributed [13] as shown in figure 5a which shows a Rayleigh distribution probability plot for image intensity in a region of coherent speckle. Due to the nature of speckle noise, multiple independent FMCs are required to calculate its statistical properties at any one image location. In figure 5a, the image intensity values are obtained from a 3mm x 3mm windowed region (625 pixels) in the L-L view centred at the centroid of the ROI with values taken from 9 independent FMCs (5625 data points in total).

In figure 5b, the RMS intensity values are plotted for the whole L-L view ROI, using the 9 independent FMC datasets, and it can be seen that the result is not spatially uniform. One approach to determining the spatial-distribution would be to make no prior assumptions and simply acquire sufficient independent FMC datasets to provide an accurate estimation of the RMS intensity at every image point. However, this would be time-consuming and impractical in many cases since it requires multiple independent measurements to be obtained from a defect-free sample (or from multiple identical defect-free samples). It is therefore hypothesised that an adequate approximation to the underlying spatial variation in RMS speckle intensity in the artefact-free region of a view can be achieved through the use of a 2D linear fit on a log (dB) scale, also shown in the figure. This empirical approach is chosen based on signal attenuation rather than beam spread being the dominant amplitude loss mechanism at the propagation distances of interest. The spatial speckle variation within the image is assessed relative to the centroid, $\bar{\mathbf{r}}$, of the ROI. The planar correction, which is applied independently for each view, is determined by fitting
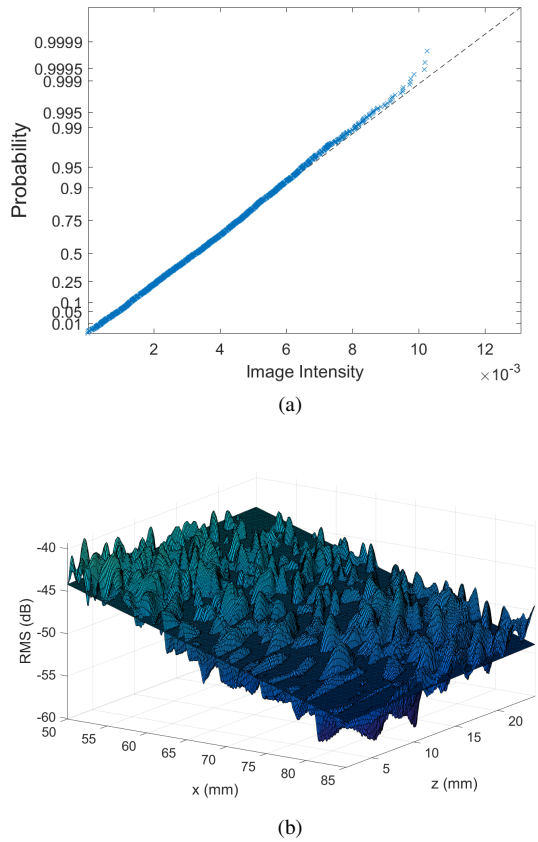
(a)

(b)

Fig. 5. Coherent grain noise in L-L view using 9 independent FMCs a) Rayleigh distribution probability plot for 3mm x 3mm box. b) Spatial variation of RMS intensities (dB) for whole ROI

$$c(\mathbf{r}) = \mathbf{m}(\mathbf{r} - \bar{\mathbf{r}}) + k \qquad (9)$$

to the image intensities (dB) where $\mathbf{m}$ denotes the gradients of the fitted plane and k the intensity at the centroid. In the case of multiple FMC datasets, each $\mathbf{r}$ is associated with multiple image intensities (one from each dataset), which contribute to the normalisation and fitting process as additional data points. The re-scaled image intensities are then determined using the planar weighting

$$I_c(\mathbf{r}) = \frac{|I(\mathbf{r})|}{10^{\frac{c(\mathbf{r})-k}{20}}} \qquad (10)$$

By accounting for the spatial variation, the speckle can be modelled as a single Rayleigh distribution, allowing for pixel information over the whole ROI to be combined, with the Rayleigh parameter determined using

$$\sigma = \sqrt{\frac{1}{2A} \int_A |I_c(\mathbf{r})|^2 d\mathbf{r}} \qquad (11)$$

where A is the image area.

Using the L-L view as an example, the combined pixel data for the 9 FMC datasets before and after applying the planar correction is shown in the probability plot in figure 6 for the complete ROI of the view. Also shown in the figure is a measure for quantitatively assessing the quality of fit to the

specified probability distribution. The red dashed lines denote the steepest gradient line which keeps all data to the right and the minimum gradient line which keeps all data to the left, the lines in both cases passing through the origin. A smaller range between the red lines indicates a better fit. The quality of fit is assessed by the difference in gradient between the bounding lines using the parameter $b = 20log_{10}(\xi_U/\xi_L)$, where ξ_U and ξ_L are the gradients of the upper and lower bounding lines respectively. From figure 6 it can be seen that the plane adjusted intensities are a good fit to the expected $y = x$ (black dashed-line) Rayleigh distribution with $b = 0.8dB$, whilst the non-corrected data displays obvious deviation and a worse fit of $b = 5.3dB$. This validates the use of 2D planar weighting as a means of accounting for the spatial variation in the speckle. A possible use of the noise characterisation procedure is to estimate the false call rate (FCR) in an image for a given detection threshold, i.e. the probability that noise in a defect-free component exceeds the detection threshold. In the remainder of the paper, a maximum allowable FCR of 0.01% is considered, which is equivalent to a detection threshold set at 4.3σ (equivalent to 10dB above the RMS noise level) for Rayleigh distributed speckle noise. In figure 6, this detection threshold level is indicated by ξ. Using the bounding fit line with the lower gradient from the bounding fit assessment enables a conservative estimate to be made of the threshold, ξ_U, needed to guarantee that the FCR does not exceed a certain level.

C. Image feature detection

The modelling of the spatial variation across the image as a 2D plane assumes gradual changes only within the image and does not account for the presence of artefacts which would distort the plane correction $c(\mathbf{r})$. Thus, prior to fitting of this plane to complete images, pixels associated with unwanted features or artefacts must be removed.

As previously noted in the description of the multi-view TFM method in section II, artefacts due to signal responses from other ray paths may be present in the region of interest. Signal responses of features (e.g. backwall) may also be present. For grain noise quantification, both can be deemed features that need to be masked. Feature detection is a common approach used by numerous disciplines to facilitate computer vision [21]–[23], although only modest research has been conducted on ultrasound feature detection, with the focus being on medical imaging [24]–[26]. Seo and Yen [27] developed a medical imaging grain-feature suppression technique called the dual apodization with cross-correlation (DAX) method. It has since been adapted by Lardner *et al.* for NDE [28]. Auto-correlation has been previously utilised for the study of random noise properties within medical B-scan imaging by Wagner *et al.* [13]. Follow on research examined the auto-correlation length for coherent speckle in medical imaging [29], although not from the perspective of feature detection.

It is hypothesised that grain speckle can be separated from unwanted coherent noise features using a physics-based detection method incorporating a combination of the properties of local auto-correlation and cluster suppression.
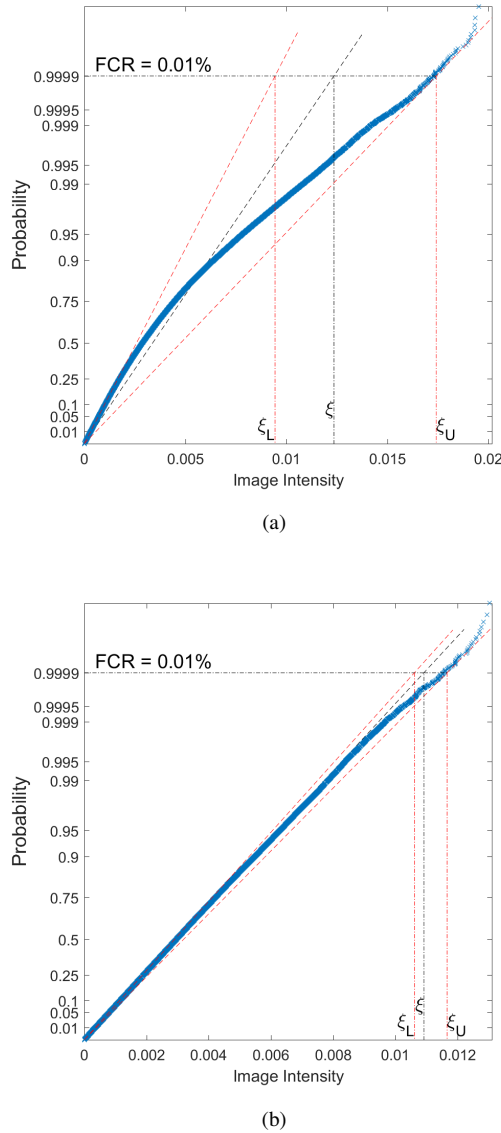
(a)

(b)

Fig. 6. Probability plot of image intensities L-L view from 9 independent FMC datasets, of a) original data and b) with spatial-correction

1) Image auto-correlation: Image auto-correlation is the process of comparing all pixel values in an image (subset) with an identical version of the image (subset) that has been translated by a given directional vector. In mathematical terms, the auto-correlation function (ACF) is defined as

$$Q(\mathbf{q}) = \int_A \bar{I}(\mathbf{r})\bar{I}(\mathbf{r} - \mathbf{q})d\mathbf{r} \qquad (12)$$

where $Q(\mathbf{q})$ denotes the value of the auto-correlation function when the translated image has been shifted by $\mathbf{q} = [a, b]$ and $\bar{I} = I_c - \frac{1}{A}\int_A I_c(\mathbf{r})d\mathbf{r}$. To utilise the ACF, it is necessary to normalise the result. Since only the magnitude of correlation is of concern, the function employed is

$$\bar{Q}(\mathbf{q}) = \frac{\|Q(\mathbf{q})\|}{\|Q_{00}\|} \qquad (13)$$

where Q_{00} denotes the auto-correlation function with no translation between images. Thus the ACF will range between [0,1],

with higher values denoting a greater correlation between the two images. The ACF analyses the shape of patterns within the image, rather than the values themselves. To quantify the information in the ACF, the scalar auto-correlation length (ACL) quantity, h, is defined as the maximum distance an image can be translated whilst maintaining a correlation coefficient greater than a given threshold, with the threshold specified here as 1/e [30], [31].

Since this is an area-based feature detection method, to provide local information it is necessary to subdivide the overall TFM image. In essence, a point within the original TFM image is associated with a box window function, centred on that point. The local ACL of the image at that point is determined from the ACF of the region of the image within the box window.

To separate the grain noise response from that of an unwanted feature, the experimental ACL is compared to its expected ACL, h_s. Then

$$h/h_s > 1 \qquad (14)$$

defines locations within the image that contain unwanted features and hence need to be masked. In the presence of speckle-only noise it is assumed that $h/h_s \leq 1$. The expected value h_s is determined using the assumption that at any image point, the expected ACF of the measured speckle pattern is similar to the ACF of the imaging point spread function (PSF). With a forward model [32] based on the work of Schmerr [33], the PSF for each view can be pre-computed for a given inspection setup. The model assumes a point scatterer and accounts for beam spread, directivity and transmission/reflection coefficients. The ACF of the PSF is calculated and the expected ACL, h_s, is then computed. This procedure is repeated at different locations throughout each view, although the sampling can be relatively coarse due to gradual variation in h_s. h_s is also used to specify the box size for calculation of h, with the h_s value at a point within the TFM image (for a given view) determining the local box size for that point to be used in the calculation of h for that view.

The local image autocorrelation function is given for both the experimental and forward model at representative points in the L-L and T-T views in figure 7. The first two example points ([50mm,15mm] and [70mm,20mm]) are artefact free regions in the L-L and T-T views respectively. For this example, the box size is fixed at 3mm by 3mm, rather than using the h_s value, to demonstrate the concept. In general, the predicted ACL values are found to be somewhat larger than those measured from speckle, hence a threshold based on $h/h_s > 1$ tends to be somewhat conservative. In the last case, figures 7g-7i, an artefact is present in the T-T view, resulting in a significantly higher experimental ACL ($h = 1.44$mm).

2) Cluster suppression: Although the ACF method in the previous section examines local image properties, it is area-based, thus smoothing out details. To complete the mask, high-intensity cluster suppression (HICS) is introduced. It is assumed that if the image data is not Rayleigh distributed, this is due to the presence of a stronger signal response from an unwanted feature, thus making the near-Rayleigh distribution
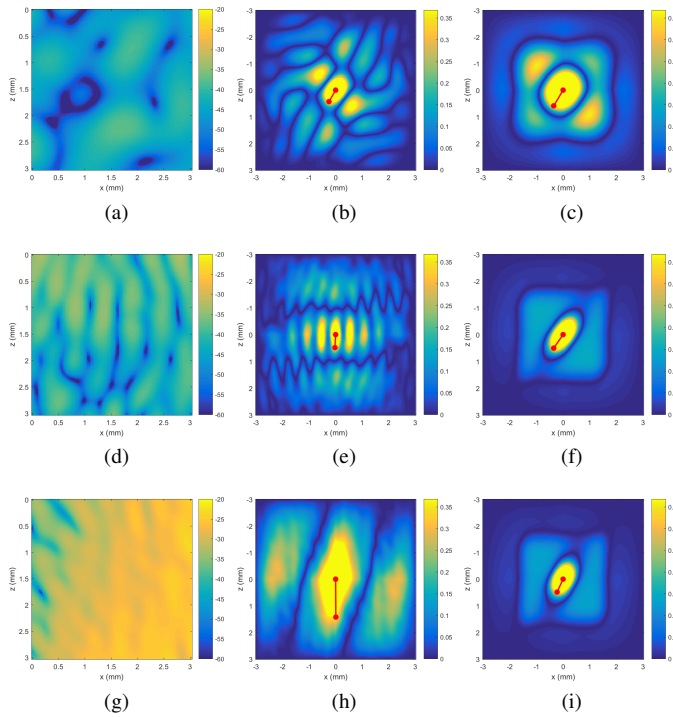
Fig. 7. Local image autocorrelation using a 3mm x 3mm box. (a)-(c) Exp TFM, Exp ACF ($h = 0.50$mm) and Expected ACF ($h_s = 0.68$mm) respectively for box centred at [50mm,15mm] in L-L view (d)-(f) same as previous, but with box centred at [70mm,20mm] in T-T view, $h = 0.49$mm, $h_s = 0.61$mm (g)-(i) box centred at [65mm,10mm] in T-T view, $h = 1.44$mm, $h_s = 0.54$mm. The ACF is thresholded at $1/e$ for visual identification of the ACL

tail-heavy (figure 8c). The procedure entails examining an image for clusters of high intensity values, and masking them.

The steps of the iterative procedure are as follows, starting from the set of points, S, remaining after performing the ACF masking method:

1) Fit a 2D plane to the non-masked image points (equation 9), where $\mathbf{r} \in S$
2) Apply planar weighting (equation 10)
3) Fit Rayleigh distribution to non-masked region of $I_c(\mathbf{r})$ using equation 11
4) From the Rayleigh CDF, calculate the Pth percentile value p
5) Find and mark the set of points $T = \{S : |I_c(\mathbf{r})| > p\}$
6) If the ratio of the set sizes T and S falls below the expected percentage (100-P), then iteration is complete
7) For each point in S, determine fraction of its neighbours also marked or masked, using box function defined by $\pm h_s$
8) Remove point with largest fraction from S and iterate

The HICS procedure requires one arbitrary parameter P, to represent the information present within the tail of the distribution, with $P = 99$ specified here. A development of an example mask is presented in figure 8 for the TT-TT view ROI. After the initial ACF masking (figures 8(c)-(d)) 10% of the ROI has been masked. The cluster suppression (figures 8(e)-(f)) completes the process, by removing a further 3% of the ROI. The complete mask has eliminated the issue

of a tail-heavy near-Rayleigh distribution without removing more information than necessary. The bounding fit range b has reduced from the non-masked 17.4dB to 8.1dB in the ACL masking stage and finally to 1.1dB in the ACL + HICS masking stage. Each mask is constructed based upon a single FMC dataset. It is worth noting that while the mask can be determined for any data set, it needs to be determined from an undamaged sample for a real inspection and then fixed during the inspection otherwise it will potentially mask signals from defects as well as artefacts.
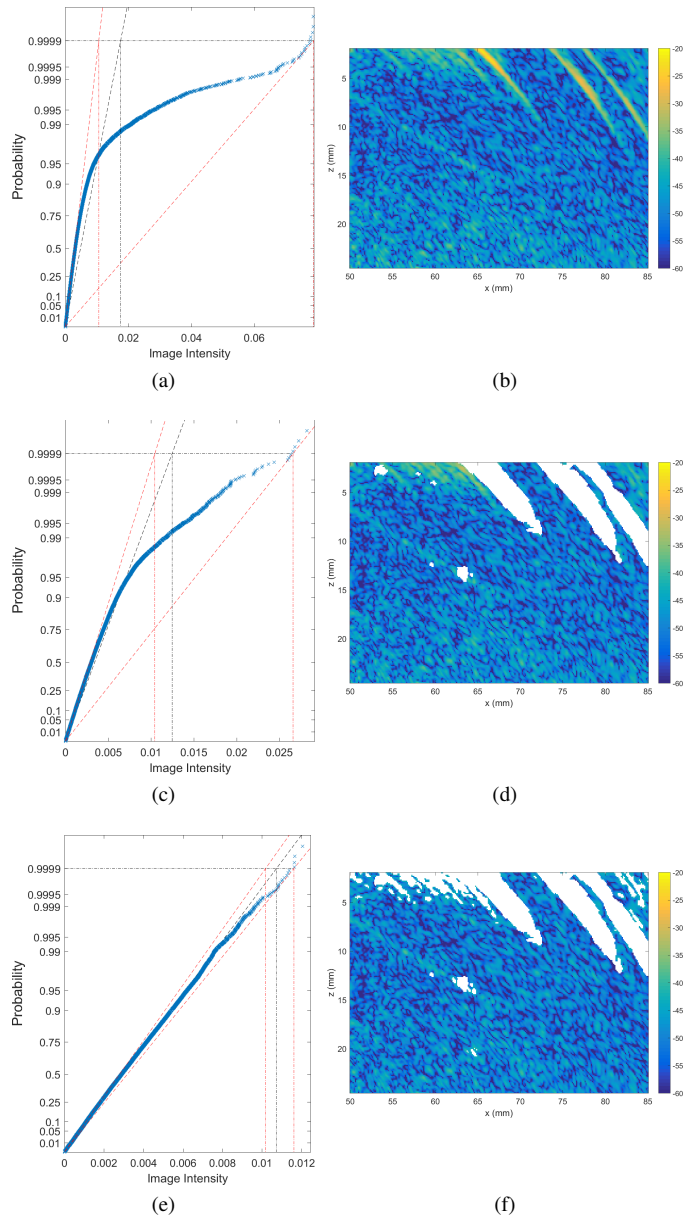
Fig. 8. Masking of the TT-TT view ROI. Rayleigh probability plots are accompanied by their respective non-masked ROI, c.f. figure 2. a)-b) No-mask, c)-d) ACF only mask, e)-f) ACF and HICS mask

The effect of image masking on the bounding fit range b is summarised in table II for all 21 views, which also shows the percentage of the ROI masked in each view. In 50% of the views, less than 1.1% of the ROI is masked. In the worst case, T-T required 18.2% of the image to be masked, due to

TABLE II
MASK PERFORMANCE FOR ROI FOR ALL 21 TFM IMAGE VIEWS

View	Masked (%)	b, no mask (dB)	b, with mask (dB)
L-L	0.6	2.3	1.4
L-T	6.8	1.4	1.3
T-T	18.2	5.9	1.3
LL-L	3.2	3.1	1.1
LL-T	2.3	3.4	1.3
LT-L	1.1	1.7	1.8
LT-T	1.5	1.6	1.3
TL-L	0.9	2.7	1.1
TL-T	2.0	1.6	0.7
TT-L	0.1	0.8	0.8
TT-T	0.7	1.0	0.5
LL-LL	0.5	1.0	1.0
LL-LT	0.4	1.4	2.0
LL-TL	0.4	1.0	1.1
LL-TT	0.2	1.3	1.3
LT-LT	5.2	7.1	1.0
LT-TL	2.6	8.4	2.0
LT-TT	0.5	1.0	0.7
TL-LT	15.9	16.5	0.5
TL-TT	0.7	1.4	0.8
TT-TT	12.9	17.4	1.1
Median	1.1	1.6	1.1

TABLE III
STATISTICAL RAYLEIGH σ PARAMETER AND FIT PARAMETER b (BOTH IN dB) FOR MULTI-VIEW IMAGES, RELATIVE TO THE PEAK L-L BACKWALL FOR INCREASING MULTIPLE INDEPENDENT FMC DATASETS. THE TABLE ALSO INCLUDES THE MEDIAN ERROR, $\Delta\sigma$, (RELATIVE TO THE 9 FMC DATASET CASE) IN σ AND THE MEDIAN BOUNDING FIT

View	1 FMC		2 FMCs		3 FMCs		9 FMCs	
	σ (dB)	b (dB)	σ (dB)	b (dB)	σ (dB)	b (dB)	σ (dB)	b (dB)
L-L	-52.3	1.4	-52.1	1.5	-52.0	1.4	-51.9	0.6
L-T	-52.1	1.1	-52.5	1.1	-52.6	1.0	-52.4	0.9
T-T	-42.6	1.6	-42.9	1.5	-42.8	1.2	-43.0	1.0
LL-L	-55.7	1.0	-55.7	0.6	-55.5	0.7	-55.3	1.2
LL-T	-49.7	1.7	-49.7	0.9	-49.6	0.8	-49.3	0.7
LT-L	-53.7	1.8	-53.8	1.6	-53.5	1.2	-53.4	3.1
LT-T	-47.8	1.3	-47.7	0.9	-47.8	0.7	-47.7	2.2
TL-L	-57.2	1.5	-57.4	1.1	-57.5	0.6	-57.3	0.5
TL-T	-53.5	1.0	-53.4	0.8	-53.4	0.7	-53.2	1.3
TT-L	-55.6	0.8	-55.8	0.7	-55.8	0.5	-55.7	0.3
TT-T	-51.8	0.6	-51.7	0.6	-51.7	0.6	-51.7	0.5
LL-LL	-50.1	1.1	-49.9	0.9	-50.0	0.5	-49.9	0.6
LL-LT	-58.1	2.0	-58.0	0.6	-58.0	0.5	-58.0	0.3
LL-TL	-54.9	1.2	-54.8	0.8	-54.7	0.6	-54.5	1.3
LL-TT	-55.4	1.3	-55.2	0.9	-55.2	0.8	-55.1	0.3
LT-LT	-57.4	0.8	-57.5	0.5	-57.5	0.6	-57.5	0.5
LT-TL	-51.3	1.6	-51.1	1.0	-51.1	0.9	-50.9	0.5
LT-TT	-54.1	0.8	-54.1	0.9	-54.0	0.6	-54.0	0.5
TL-LT	-54.7	1.1	-55.1	1.1	-55.0	0.5	-55.0	1.8
TL-TT	-56.5	1.0	-56.5	1.6	-56.5	1.2	-56.4	0.8
TT-TT	-52.3	1.2	-52.1	1.6	-52.0	1.0	-51.9	0.8
$\Delta\sigma$	0.25	–	0.12	–	0.11	–	0.00	–
Median	–	1.20	–	0.90	–	0.67	–	0.65

the second frontwall reflection artefact. A minimal masking of the ROI allows for greater use of the remaining image data, whether as individual images or as inputs into a data fusion algorithm.

From table II, the mask performance typically results in a bounding fit range of 1.1dB, thus the non-masked region of each image distribution is in excellent agreement with the hypothesis of a Rayleigh distribution. Although the masking process is designed to improve the bounding fit range in general, it is possible for a view to have a minor negative impact as in the LL-LT case in this instance. The bounding fit range for LL-LT has risen from 1.4 to 2.0 after masking, although this outlier has a similar fit in both instances. The fit divergence, although negligible, is primarily due to the artefact region containing fewer high percentile values than expected, effecting ξ_L (figure 9). In views which contain a strong artefact, such as T-T, TL-LT and TT-TT, the bounding fit is significantly improved through use of the mask, with the improvement ranging by up to an order of magnitude.

The advantage of the local-detection approach is that the mask is applied to a particular image view, rather than to a time-window within the raw scanline data as in [34]. As such, the information masked is more targeted, with no impact on other views.

D. Effect of reducing number of independent datasets used for noise characterisation

In section III-B, multiple independent FMC datasets were used to determine the statistical parameters of the speckle noise. This section examines a more efficient means of gathering these parameters, and determines the minimum number of independent FMC datasets required.

In table III, the improvement obtained by increasing the number of independent FMC datasets used to construct the statistical Rayleigh parameter σ is presented. From the table it is evident that the increased FMC dataset count has negligible impact on the speckle noise parameter, even in the presence of artefacts. With only a single FMC dataset, the estimated σ is within 0.4dB of that calculated using 9 FMC datasets for all views, with the average error being 0.25dB and the worst being the LT-L view. The median error in the Rayleigh parameter (relative to the 9 FMC dataset case) decreases steadily as the number of FMC datasets is increased. The bounding fit parameter b also displays the same general trend, although for the LT-L view, the expected improvement from combining multiple FMC datasets is not as evident, due to the masking process failing to completely remove a small artefact near the backwall in the fifth FMC dataset.

Therefore, the number of FMC datasets required to quantify the speckle noise is only one, as the independent information present within an image view is sufficient to characterise the noise, even in the presence of unwanted artefacts. The final noise parameters, for both the random and speckle noise are given in figure 9 for each view. Due to the number of averages utilised, the random noise level was less than -59dB relative to the peak backwall response from the L-L view. The FCR 0.01% speckle noise at the centre of the ROI ranged from -30 to -45dB over all 21 views.

IV. SUMMARY OF PROPOSED NOISE CHARACTERISATION PROCEDURE FOR MULTI-VIEW TFM IMAGES

In brief, the experimental procedure entails the following steps:

1) Pre-calculate the modelled auto-correlation lengths h_s of the PSF in each view as described in section III-C
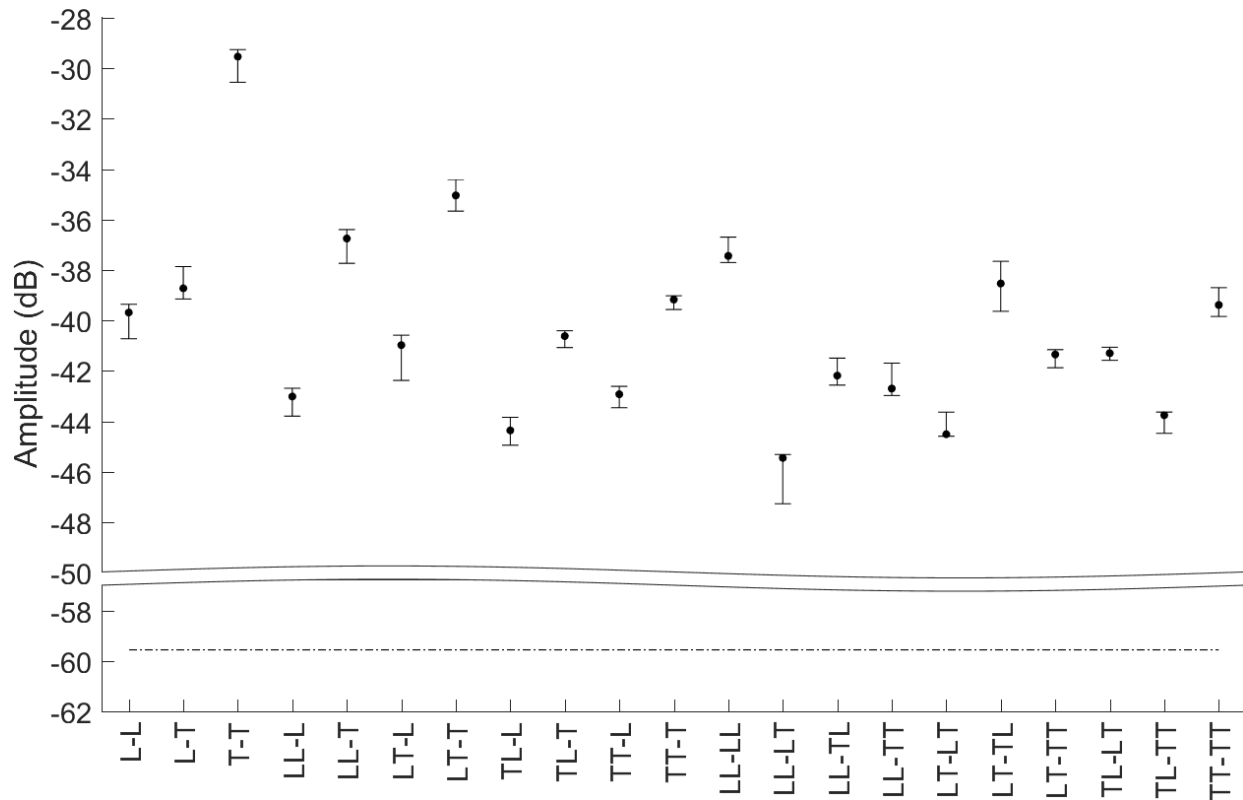
Fig. 9. Random and speckle noise quantities for each view image, relative to peak backwall reflection in L-L view. Dashed line is the random noise, with points denoting speckle noise, at FCR 0.01% (RMS + 10dB). The error bars denote the speckle noise conservative fit range b

2) Collect averaged FMC from an undamaged sample and process the data using multi-view TFM imaging algorithm (equation 1). Since the random noise suppression required cannot be assessed prior to calculation of speckle noise, it is recommended that a conservative choice for the number of averages is made at this stage, e.g. 10-20

3) Determine the random noise level using the back-to-back paired FMC approach (with no averaging) for a single measurement location using equation 6

4) Remove image artefacts using masking procedure of section III-C

5) Adjust non-masked points for spatial variation in Rayleigh distribution (equations 9 and 10)

6) Determine image level Rayleigh parameter σ for each view on non-masked points using maximum likelihood estimation (equation 11)

7) Confirm number of averages is sufficient for random noise suppression relative to the image speckle noise (in view with lowest speckle noise level), if not, use equation 8 to estimate required number of averages and repeat steps 2-6 above

8) Assess outcome using Rayleigh probability plots on non-masked data

V. Conclusions

A procedure for the efficient determination of ultrasonic image noise has been proposed, which uses experimental based

characterisation to quantify the random and micro-structure grain noise. To determine the random noise, only a pair of FMC datasets captured in succession are required. For the grain-induced speckle noise, instead of relying on many independent FMC datasets from pristine samples to obtain pixel-by-pixel noise parameters, the procedure assumes consistent linear spatial variation within each image. This enables intra-image information to be combined, which reduces the number of independent FMC datasets required. This procedure was applied to direct, half-skip and full-skip images constructed using the multi-view TFM algorithm. To mitigate the impact of image artefacts and unwanted features, a process was developed which incorporated expected local auto-correlation length and high amplitude cluster suppression. The masking process requires the simulation of the inspection setup to predict the expected ACL from the PSF in each image. A simple ray-based forward model was shown to be sufficient for this purpose, and only needs to be executed once for a given inspection configuration. It was demonstrated that the masking procedure was effective, with typically only 0.5% to 3.7% (25th and 75th percentiles) of the region of interest needing to be masked in order to leave the intensity in the non-masked region closely following a Rayleigh distribution.

The procedure outlined is highly efficient, with only a single FMC dataset required to obtain a good estimate of the true noise parameters. In the example case, speckle noise parameters estimated from a single FMC dataset for 21 multi-view images were on average within 0.2dB of those obtained

from 9 independent FMC datasets. Since the procedure of noise quantification outlined in the paper is independent of the imaging algorithm, it can also be readily applied to other imaging algorithms for the purpose of determining the noise component of the signal-to-noise ratio for use in a data fusion algorithm.

DATA ACCESS STATEMENT

All data used in this paper are openly available for download from the University of Bristol Research Data Repository at https://doi.org/10.5523/bris.38wvyorif7v5a27ohkiw5mvmof

REFERENCES

[1] C. Holmes, B. W. Drinkwater, and P. D. Wilcox, "Post-processing of the full matrix of ultrasonic transmit-receive array data for non-destructive evaluation," *NDT & E International*, vol. 38, no. 8, pp. 701–711, 12 2005.

[2] B. W. Drinkwater and P. D. Wilcox, "Ultrasonic arrays for non-destructive evaluation: A review," *NDT & E International*, vol. 39, no. 7, pp. 525–541, 10 2006.

[3] A. J. Hunter, B. W. Drinkwater, and P. D. Wilcox, "The wavenumber algorithm for full-matrix imaging using an ultrasonic array," *IEEE Transactions on Ultrasonics, Ferroelectrics, and Frequency Control*, vol. 55, no. 11, pp. 2450–2462, 11 2008.

[4] J. Zhang, B. W. Drinkwater, and P. D. Wilcox, "Efficient immersion imaging of components with non-planar surfaces," *IEEE Trans. Ultrason. Ferr. Freq. Contr.*, vol. 61, no. 8, pp. 1284–1295, 2014.

[5] J. Zhang, T. Barber, A. Nixon, and P. Wilcox, "Investigation into distinguishing between small volumetric and crack-like defects using multi-view total focusing method images," *AIP conference proceedings*, vol. 1806, p. 040003, 2017.

[6] J. Zhang, B. W. Drinkwater, P. D. Wilcox, and A. J. Hunter, "Defect detection using ultrasonic arrays: The multi-mode total focusing method," *NDT & E International*, vol. 43, no. 2, pp. 123 – 133, 3 2010.

[7] Z. Wang, J. Li, and R. Wu, "Time-delay- and time-reversal-based robust capon beamformers for ultrasound imaging," *IEEE Transactions On Medical Imaging*, vol. 24, pp. 1308–1322, 2005.

[8] S. Park, A. B. Karpiouk, and S. R. Aglyamov, "Adaptive beamforming for photoacoustic imaging using linear array transducer," *IEEE International Ultrasonics Symposium Proceedings*, vol. 1088-1091, 2008.

[9] G. Matrone, A. S. Savoia, G. Caliano, and G. Magenes, "The delay multiply and sum beamforming algorithm in ultrasound b-mode medical imaging," *IEEE Transactions On Medical Imaging*, vol. 34, pp. 940–949, 2015.

[10] M. Li and G. Hayward, "Optimal matched filter design for ultrasonic NDE of coarse grain materials," *42nd Annual Review of Progress in Quantitative Nondestructive Evaluation*, vol. 1706, pp. 020 011–1–9, 2016.

[11] C. Burckhardt, "Speckle in ultrasound b-mode scans," *IEEE Transactions on Sonics and Ultrasonics*, vol. SU-25, no. 1, pp. 1–6, 1978.

[12] G. E. Trahey, S. W. Smith, and O. T. V. Ramm, "Speckle pattern correlation with lateral aperture translation: Experimental results and implications for spatial compounding," *IEEE Trans. Ultrason. Ferr. Freq. Contr.*, vol. 33, no. 3, pp. 257–264, 1986.

[13] R. F. Wagner, S. W. Smith, J. M. Sandrik, and H. Lopez, "Statistics of speckle in ultrasound b-scans," *IEEE Transactions On Sonics And Ultrasonics*, vol. 30, pp. 156–163, 1983.

[14] D. C. Crawford, D. S. Bell, and J. C. Bamber, "Compensation for the signal processing characteristics of ultrasound b-mode scanners in adaptive speckle reduction," *Ultrasound in Med. & Biol.*, vol. 19, no. 6, pp. 469–485, 1993.

[15] X. Gros, Z. Liu, K. Tsukada, and K. Hanasaki, "Experimenting with pixel-level NDT data fusion techniques," *IEEE Transactions On Instrumentation And Measurement*, vol. 49, no. 5, pp. 1083–1089, 2000.

[16] Z. Liu, D. S. Forsyth, J. P. Komorowski, K. Hanasaki, and T. Kirubarajan, "Survey: State of the art in NDE data fusion techniques," *IEEE Transactions On Instrumentation And Measurement*, vol. 56, no. 6, pp. 2435–2451, 2007.

[17] N. Brierley, T. Tippetts, and P. Cawley, "Data fusion for automated non-destructive inspection," *Proceedings of the Royal Society A*, vol. 470, no. 2167, 2014.

[18] A. Ben-Menahem and S. J. Singh, *Seismic Waves and Sources*. Springer-Verlag, 1981.

[19] J. S. Bendat and A. G. Piersol, *Random Data*. New York: Wiley, 2000.

[20] P. Beckmann, "Rayleigh distributions and its generalizations," *Radio Science*, vol. 68D, no. 9, pp. 927–932, 1964.

[21] R. M. Haralick, "Statistical and structural approaches to texture," *Proceedings of the IEEE*, vol. 67, no. 5, pp. 786–804, May 1979.

[22] T. Kurita, N. Otsu, and T. Sato, "A face recognition method using higher order local autocorrelation and multivariate analysis," in *Proceedings., 11th IAPR International Conference on Pattern Recognition. Vol.II. Conference B: Pattern Recognition Methodology and Systems*, Aug 1992, pp. 213–216.

[23] B. Zitova and J. Flusser, "Image registration methods: a survey," *Image and Vision Computing*, vol. 21, pp. 977–1000, 2003.

[24] H. D. Cheng, J. Shan, W. Ju, Y. Guo, and L. Zhang, "Automated breast cancer detection and classification using ultrasound images: A survey," *Pattern Recognition*, vol. 43, no. 1, pp. 299 – 317, 2010.

[25] I. Hacihaliloglu, R. Abugharbieh, A. J. Hodgson, R. N. Rohling, and P. Guy, "Automatic bone localization and fracture detection from volumetric ultrasound images using 3-d local phase features," *Ultrasound in Medicine & Biology*, vol. 38, no. 1, pp. 128 – 144, 2012.

[26] F. C. Cruz, E. F. S. Filho, M. C. S. Albuquerque, I. C. Silva, C. T. T. Farias, and L. L. Gouvêa, "Efficient feature selection for neural network based detection of flaws in steel welded joints using ultrasound testing," *Ultrasonics*, vol. 73, pp. 1 – 8, 2017.

[27] C. H. Seo and J. T. Yen, "Sidelobe suppression in ultrasound imaging using dual apodization with cross-correlation," *IEEE Transactions on Ultrasonics, Ferroelectrics, and Frequency Control*, vol. 55, no. 10, pp. 2198–2210, October 2008.

[28] T. Lardner, M. Li, R. Gongzhang, and A. Gachagan, "A new speckle noise suppression technique using cross-correlation of array sub-apertures in ultrasonic NDE of coarse grain materials," *39th Annual Review of Progress in Quantitative Nondestructive Evaluation*, vol. 1511, pp. 865–871, 2013.

[29] R. F. Wagner, M. F. Insana, and S. W. Smith, "Fundamental correlation lengths of coherent speckle in medical ultrasonic images," *IEEE Transactions On Ultrasonics Ferroelectrics And Frequency Control*, vol. 35, pp. 34–44, 1988.

[30] J. A. Ogilvy and J. R. Foster, "Rough surfaces: Gaussian or exponential statistics?" *J. Phys. D*, vol. 22, pp. 1243–1251, 1989.

[31] F. Daly, D. J. Hand, M. C. Jones, A. D. Lunn, and K. J. McConway, *Elements of Statistics*. New York, NY: Addison-Wesley, 1997.

[32] N. Budyn, R. Bevan, A. Croxford, J. Zhang, P. Wilcox, A. Kashubin, and P. Cawley, "Sensitivity images for multi-view ultrasonic array inspection," in *AIP Conference Proceedings*, vol. 1949, no. 1. AIP Publishing, 2018, p. 080001.

[33] L. W. Schmerr, *Fundamentals of Ultrasonic Phased Arrays*. Springer International Publishing, 2015.

[34] E. Iakovleva, S. Chatillon, P. Bredif, and S. Mahaut, "Multi-mode TFM imaging with artefacts filtering using CIVA UT forwards models," *40th Annual Review of Progress in Quantitative Nondestructive Evaluation*, vol. 1581, pp. 72–79, 2014.